

## RESEARCH ARTICLE

10.1002/2015JD024150

## Key Points:

- Passage of a CCKW is associated with coherent atmosphere-ocean interactions that last about 4 days
- Upper ocean temperature diurnal cycle is suppressed and bulk SST is decreased during CCKW event
- Air-sea interactions during CCKW passage are substantial contributor to intraseasonal variability

## Correspondence to:

D. B. Baranowski,  
dariusz.b.baranowski@jpl.nasa.gov

## Citation:

Baranowski, D. B., M. K. Flatau, P. J. Flatau, and A. J. Matthews (2016), Impact of atmospheric convectively coupled equatorial Kelvin waves on upper ocean variability, *J. Geophys. Res. Atmos.*, *121*, 2045–2059, doi:10.1002/2015JD024150.

Received 28 AUG 2015

Accepted 16 JAN 2016

Accepted article online 22 JAN 2016

Published online 4 MAR 2016

## Impact of atmospheric convectively coupled equatorial Kelvin waves on upper ocean variability

Dariusz B. Baranowski<sup>1,2</sup>, Maria K. Flatau<sup>3</sup>, Piotr J. Flatau<sup>4</sup>, and Adrian J. Matthews<sup>5</sup>

<sup>1</sup>Institute of Geophysics, Faculty of Physics, University of Warsaw, Warsaw, Poland, <sup>2</sup>Joint Institute for Regional Earth System Science and Engineering, University of California, Los Angeles, California, USA, <sup>3</sup>Naval Research Laboratory, Marine Meteorology Division, Monterey, California, USA, <sup>4</sup>Scripps Institution of Oceanography, La Jolla, California, USA, <sup>5</sup>Centre for Ocean and Atmospheric Sciences, School of Environmental Sciences and School of Mathematics, University of East Anglia, Norwich, UK

**Abstract** Convectively coupled Kelvin waves (CCKWs) are atmospheric weather systems that propagate eastward along the equatorial wave guide with phase speeds between 11 and 14 m s<sup>-1</sup>. They are an important constituent of the convective envelope of the Madden-Julian oscillation (MJO), for which ocean-atmosphere interactions play a vital role. Hence, ocean-atmosphere interactions within CCKWs may be important for MJO development and prediction and for tropical climate, in general. Although the atmospheric structure of CCKWs has been well studied, their impact on the underlying ocean is unknown. In this paper, the ocean-atmosphere interactions in CCKWs are investigated by a case study from November 2011 during the CINDY/DYNAMO field experiment, using in situ oceanographic measurements from an ocean glider. The analysis is then extended to a 15 year period using precipitation data from the Tropical Rainfall Measuring Mission and surface fluxes from the TropFlux analysis. A methodology is developed to calculate trajectories of CCKWs. CCKW events are strongly controlled by the MJO, with twice as many CCKWs observed during the convectively active phase of the MJO compared to the suppressed phase. Coherent ocean-atmosphere interaction is observed during the passage of a CCKW, which lasts approximately 4 days at any given longitude. Surface wind speed and latent heat flux are enhanced, leading to a transient suppression of the diurnal cycle of sea surface temperature (SST) and a sustained decrease in bulk SST of 0.1°C. Given that a typical composite mean MJO SST anomaly is of the order of 0.3°C, and more than one CCKW can occur during the active phase of a single MJO event, the oceanographic impact of CCKWs is of major importance to the MJO cycle.

### 1. Introduction

Convectively coupled Kelvin waves (CCKWs) are an important part of the atmospheric equatorial dynamics. Near the equator, CCKWs are the leading modes of eastward moving convection on time scales between several days and 3 weeks [Kiladis *et al.*, 2009]. CCKWs, together with other equatorial eastward and westward propagating perturbations form the “building blocks” of the multiscale structure in the active phase of the Madden-Julian oscillation (MJO) [Majda and Khouider, 2004; Mapes *et al.*, 2006]. Their importance was first recognized by Nakazawa [1988], who noticed the eastward moving cloud “superclusters” embedded in the MJO envelope. CCKWs can be separated from the MJO by their phase speed, which is faster than that of the MJO [Straub and Kiladis, 2002; Wheeler and Kiladis, 1999]. While the phase speed of the MJO observed in the Indian Ocean is about 4–5 m s<sup>-1</sup>, the phase speeds of convectively coupled Kelvin waves in this region range from about 14 m s<sup>-1</sup> for suppressed MJO condition to 11 m s<sup>-1</sup> during the convective phase of the MJO [Roundy, 2008].

The MJO itself strongly affects ocean variability, and air-sea interaction is one of the mechanisms contributing to MJO development and propagation [Flatau *et al.*, 1997; Flatau *et al.*, 2003; Fu and Wang, 2004; Shinoda *et al.*, 1998]. During the active phase of the MJO, increased convective activity leads to reduced shortwave radiation (through increased cloudiness), enhanced surface latent, and sensible heat fluxes (mainly due to increased wind speed), and enhanced upper ocean mixing. These processes cool the ocean surface. Ahead of the propagating MJO system, the large solar radiative fluxes and weak surface heat fluxes lead to increased ocean temperature associated with large diurnal SST variability [Shinoda *et al.*, 2013]. This diurnal SST warming influences the distribution of tropical precipitation contributing to the coupled feedbacks between ocean and atmosphere that maintain the basic state, the timing of the seasonal cycle of SST, and the trade winds in the tropical Pacific [Bernie *et al.*, 2008]. The impact of the diurnal variability represented by a skin layer prognostic scheme [Zeng and Beljaars, 2005] on the modeled tropical convection can be observed

[McLay *et al.*, 2012]. Including the diurnal variability of SST in the global model ensembles improves the model precipitation pattern, diurnal variability of precipitation, and ensemble spread. In a full dynamical ocean model or ocean mixed layer model coupled with an atmospheric GCM, increased resolution of the oceanic mixed layer leads to better representation of the diurnal SST variability and improved MJO forecasts [Woolnough *et al.*, 2007]. Also, resolving diurnal SST variability improves simulations of other tropical phenomena such as the Indian summer monsoon [Klingaman *et al.*, 2011].

Similar air-sea interaction mechanisms to those in the MJO may operate during the passage of the CCKWs. On the faster CCKW time scale (a few days) the upper ocean processes and diurnal variability are especially important, and the purpose of this paper is to investigate the impact of CCKWs on the upper ocean behavior. To this end we use a simple predictive model of the existence and strength of the oceanic diurnal surface warm layer [Matthews *et al.*, 2014], using high-resolution ocean glider measurements from the Dynamics of the Madden Julian Oscillation (DYNAMO) period and TropFlux gridded solar radiation flux and wind speed products. Investigations of the ocean glider measurements of the upper ocean from DYNAMO [Matthews *et al.*, 2014] indicate that the diurnal warm layer developed during periods of daily mean low wind speed ( $<6 \text{ m s}^{-1}$ ) and high solar insolation ( $>80 \text{ W m}^{-2}$ ). Although diurnal warm layers were observed during both active and suppressed MJO phases, they were more frequent during the suppressed MJO phase.

During the DYNAMO period (October 2011 to February 2012), 15 CCKWs were identified, with exceptionally strong “double barrel” waves related to the November 2011 MJO episode [Johnson and Ciesielski, 2013]. Nine of these events were associated with the active phase of the MJO, while seven developed during the suppressed phase [Gottschalck *et al.*, 2013]. Radar observations were used to analyze the difference in structure and intensity of the CCKWs during the suppressed and active phases of the MJO in DYNAMO [DePasquale *et al.*, 2014]. In the active phase, the waves were more intense with higher moisture and more clouds, possibly impacting the radiative effects of the wave. In the suppressed MJO phase, the waves developed in a drier atmosphere and therefore were less intense. In these waves, unlike in the waves associated with the active MJO, moisture buildup ahead of the convective activity appeared to play a role in the wave development.

This paper investigates the variability of the surface ocean and its diurnal cycle over the Indian Ocean during the passage of CCKWs observed in DYNAMO, and then extends the investigation to a 15 year period, for which diurnal warm layer strength was diagnosed using the TropFlux ocean surface fluxes and DYNAMO-derived deterministic model [Matthews *et al.*, 2014]. Individual CCKW trajectories were calculated using Tropical Rainfall Measuring Mission (TRMM) precipitation data, enabling a Lagrangian analysis of the interaction between CCKWs and the ocean surface.

The structure of the paper is as follows. Section 2 presents the data sets and methodology used in this study; Section 3 describes the variability of SST, wind speed, and latent heat flux at the ocean surface during CCKW passage during the November 2011 MJO event in DYNAMO [Johnson and Ciesielski, 2013]; Section 4 describes a composite analysis based on a newly developed, 15 year CCKW climatology; Section 5 is the summary and discussion.

## 2. Methodology

### 2.1. Precipitation Data and Kelvin Wave Filtering

The primary data set used to determine the CCKW trajectories consists of 15 years of gridded estimates of precipitation from the TRMM merged product 3B42 (version 7) [Huffman *et al.*, 2007] from January 1998 to December 2013. The temporal resolution is 3 h, enabling the analysis of the diurnal cycle. Spatial resolution is  $0.25^\circ$  in both longitude and latitude. Kelvin waves are symmetric around the equator and constrained to the proximity of the equator over the Indian Ocean region [Kiladis *et al.*, 2009]. Hence, the precipitation data are averaged from  $2.5^\circ\text{S}$  to  $2.5^\circ\text{N}$ , to create a two-dimensional (longitude-time) precipitation data set. This is referred to as the “unfiltered” TRMM data set and contains variability from many different equatorial modes.

To isolate the CCKW precipitation from the “unfiltered” TRMM data set, wave number frequency filtering is performed. Following Wheeler and Kiladis [1999], the data set is first transformed into the wave number frequency domain using a two-dimensional fast Fourier transform (FFT). The wave number frequency data are then filtered, only retaining variability corresponding to CCKWs, i.e., waves with eastward phase speeds between  $8$  and  $30 \text{ m s}^{-1}$ , zonal wave numbers between 1 and 14, and frequencies between  $1/30$  and

0.4 cycles per day (cpd). After a reverse FFT back to physical (longitude-time) space, this is referred to as the K14 data set. As noted by *Roundy* [2008], by using the symmetric portion of the rainfall (i.e., averaged from 2.5°S to 2.5°N), we have eliminated the signal from the eastward propagating inertia-gravity waves that are present for this wave number frequency range but that have an asymmetric convective signature about the equator.

The K14-filtered data will be used to identify individual CCKW trajectories, whereas the unfiltered precipitation data will be used to check the proposed method. Given the range of phase speeds of the CCKWs ( $8 - 30 \text{ m s}^{-1}$ ) and the temporal resolution of the data (3 h), the minimum effective zonal resolution is approximately 1°. Hence, the unfiltered and K14 data are averaged in the zonal dimension into 1° grid boxes.

## 2.2. CCKW Trajectory Database

The K14-filtered data set is used to create a database of CCKW activity. First, a binary “Eulerian” database of CCKWs is created. A two-dimensional (1° longitude, 3 h time) grid, the same size as the K14-filtered data, is created and populated with zeroes. For each longitude, all local maxima (in time) in the K14 data, above a threshold of  $0.15 \text{ mm h}^{-1}$ , are identified and replaced by a “1” in the database. The value of this threshold was chosen to be large enough to exclude random noise (it is above the  $0.13 \text{ mm h}^{-1}$  zonal mean value of the standard deviation of filtered precipitation) but low enough to ensure that CCKWs of moderate strength and above were included in the database.

To transform this Eulerian database into a Lagrangian framework that follows the development of a CCKW along its trajectory from beginning to end, we consider longitude boxes in close proximity to each other. We have found that at any given location, two sequential CCKWs never occur within 30 h of each other. Furthermore, phase speed of a CCKW is such that in 3 h it travels a distance of about 1°. The time required for a wave to travel between two neighboring boxes is much smaller than minimal time of reoccurrence in single location, which allows identifying signals associated with a single CCKW event. Because some CCKW events may propagate with lower phase speed, the maximum time in which signal has to be detected in the following box has been set to 6 h. Hence, if two maxima are detected in two neighboring boxes, within the 6 h timeframe, they are identified as part of a single CCKW trajectory. A trajectory calculation begins with data for which there is no preceding (within the 6 h threshold) maximum (a 1 in the binary database) in the westward neighbor of a given location. Such a point is defined as the beginning of a trajectory. The trajectory is extended eastward until there is no maximum in K14-filtered precipitation to the east of the previously CCKW-defined trajectory point. A trajectory has to last for a minimum of 12 h to be included in the database. Hence, a trajectory in the Lagrangian database consists of a contiguous sequence of 1 values in the Eulerian database, all identified as belonging to the same CCKW.

Due to the finite number of zonal wave numbers represented in the K14-filtered precipitation it is unavoidable that some trajectories are “overextended” at the beginning or end, when compared with the actual, unfiltered precipitation. To correct this, a further quality control was performed, using the unfiltered precipitation data along each CCKW trajectory. At each longitude on the trajectory, the 9 h mean of unfiltered precipitation is calculated, using data 3 h before, on the trajectory, and 3 h after. Starting at the beginning of the trajectory (its farthest westward point), two criteria need to be satisfied for that point to remain on the trajectory. First, the 9 h mean at that longitude must exceed a threshold of  $0.5 \text{ mm h}^{-1}$ . Second, a further average of this 9 h mean value, averaged over all points on the trajectory from the current point to the (eastward) point 12 h later must also exceed a threshold of  $0.25 \text{ mm h}^{-1}$ . If both these criteria are not met, the current point is ejected from the trajectory, and the analysis is repeated at the subsequent eastward point until the criteria are met. The same procedure is applied backward from the end of the trajectory. This process guarantees that the beginning and end points of the trajectories are associated with real, unfiltered precipitation signals. The numerical values of the threshold were chosen to ensure that spurious end points on the trajectories were removed, while not overpruning the trajectories. For context, the time mean precipitation over the equatorial (2.5°S to 2.5°N) belt is  $0.17 \text{ mm h}^{-1}$ .

It should be noted that the methodology described above limits our CCKW database to the continuous precipitation events associated with CCKWs, which is a subset of all CCKWs. However, the possibility that two CCKW trajectories, independent in our database, are in fact a part of the same continuous trajectory with a gap in precipitation signal that has been explored. No such cases have been found over the Indian Ocean. Therefore, for that basin, linking the beginning and end of a trajectory to the physical precipitation assures that it is indeed a coupled, precipitating event.

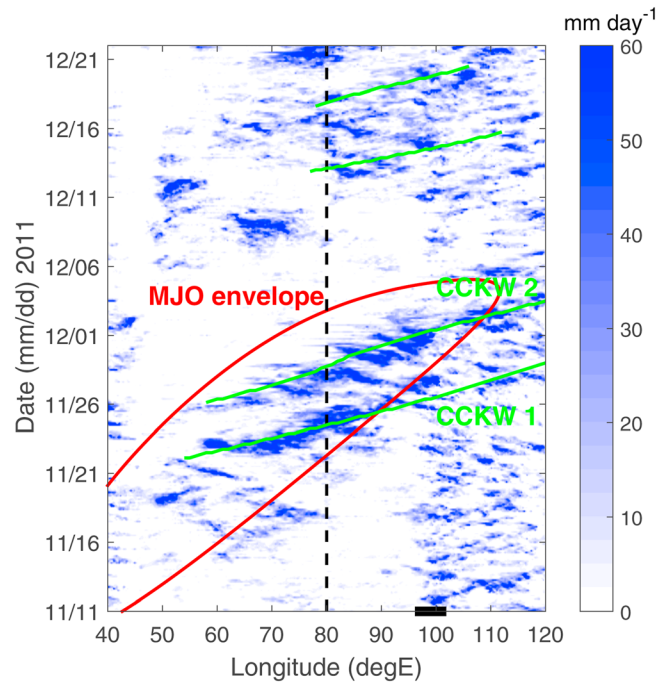


**Figure 1.** Hovmoller diagram of TRMM precipitation rate ( $\text{mm d}^{-1}$ ) over the equatorial Indian Ocean, averaged from  $2.5^{\circ}\text{S}$  to  $2.5^{\circ}\text{N}$  from 11 November to 21 December 2011, during the DYNAMO field experiment. Green lines show Kelvin wave trajectories; the red solid line indicates the envelope of the November MJO; black dashed line indicates location of the Seaglider; the black bar on the longitude axis indicates the location of Sumatra.

Example CCKW trajectories are shown for the DYNAMO period of November 2011 as green lines, superimposed over the unfiltered precipitation (Figure 1) and K14-filtered precipitation (Figure 2). The trajectories follow continuous, eastward propagating ridges (local signal maxima), which exceed the previously defined threshold of  $0.15 \text{ mm h}^{-1}$  rain rate in K14-filtered precipitation (Figure 2). Comparison with the full precipitation signal (Figure 1) shows good agreement with the trajectory calculation algorithm.

### 2.3. TropFlux Wind Speed, Latent Heat Flux, SST, Air Temperature, and Humidity Data

The TropFlux product [Praveen Kumar *et al.*, 2013] provides daily estimates of wind speed, latent heat flux (LHF), ocean temperature (SST), atmospheric temperature and humidity (both at 2 m), and solar radiation at the ocean surface, derived from ERA-interim data. The TropFlux data are available on a regular grid with  $1 \times 1^{\circ}$  spatial resolution over the

oceans. As with the TRMM precipitation data, two-dimensional (longitude-time) data sets were created by averaging over the equatorial belt ( $2.5^{\circ}\text{S}$  to  $2.5^{\circ}\text{N}$ ). Because SST exhibits a large seasonal cycle over the Indian Ocean, an SST anomaly was computed by removing the seasonal cycle (calculated as the mean plus the first three annual harmonics from the 1979–2013 data set).

### 2.4. A TropFlux-Derived Measure of the Diurnal Cycle of SST ( $T^{\dagger}$ )

Following Matthews *et al.* [2014],  $T^{\dagger}$  is defined as the difference between the current SST and the SST value at 0600 local solar time (LST), i.e., sunrise, on the same day. Hence, the daily mean value of  $T^{\dagger}$  is a measure of the strength of the diurnal cycle in SST. The algorithm developed in Matthews *et al.* [2014] to predict daily  $T^{\dagger}$  based on daily mean values of TropFlux shortwave radiation and wind speed at the ocean surface is used here. Nonlinear regression against these two variables is given by equation (18) in that paper and has the following form:

$$T^{\dagger}_{\text{predicted}} = \alpha_1 \text{SWRV} + \alpha_2 \text{SWR} + \alpha_3 V + \alpha_4,$$

where SWR is shortwave radiation flux ( $\text{W m}^{-2}$ ),  $V$  is surface wind speed ( $\text{m s}^{-1}$ ),  $\alpha_1 = -2.16 \times 10^{-4} \text{ }^{\circ}\text{C m s W}^{-1}$ ,  $\alpha_2 = 0.00208 \text{ }^{\circ}\text{C m}^2 \text{ W}^{-1}$ ,  $\alpha_3 = 0.0152 \text{ }^{\circ}\text{C s m}^{-1}$ , and  $\alpha_4 = -0.182 \text{ }^{\circ}\text{C}$ .

Although the relationship is derived using in situ ocean glider observations collected during the 4 month long period of the DYNAMO field campaign (October 2011 to January 2012), we follow the assumption introduced and explored by Matthews *et al.* [2014], that diurnal warm layer development and evolution is, to first order, controlled by wind speed and shortwave radiation flux at the ocean surface. Thus, the predictive model of  $T^{\dagger}$  should stay valid over the entire equatorial belt.

### 2.5. Ocean Glider Measurements

In situ upper ocean profiles analyzed in this study were measured by an ocean glider (Seaglider) deployed in the equatorial Indian Ocean near  $80^{\circ}\text{E}$  during DYNAMO. Quality controlled, optimally interpolated data for the period 20 November to 1 December 2011 are used here. The temporal and vertical resolutions of the

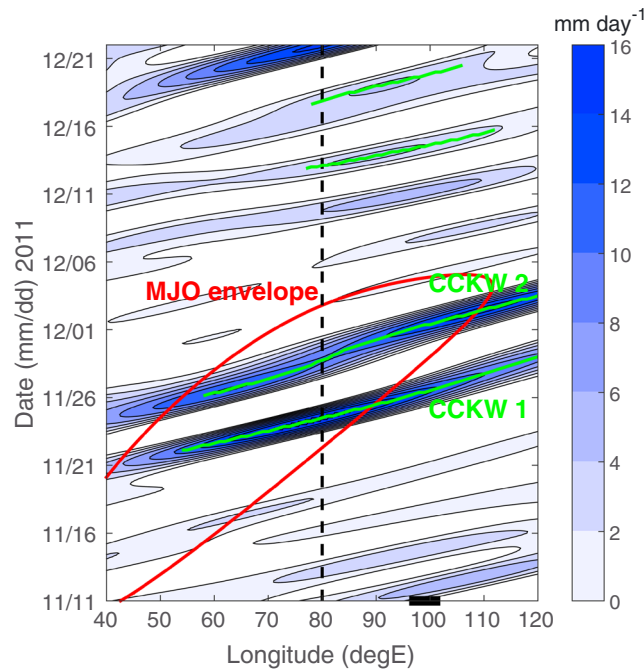


**Figure 2.** As in Figure 1 but for K14-filtered precipitation. Negative values are masked.

interpolated Seaglider data are 1 h and 0.5 m, respectively. A comprehensive description of the DYNAMO Seaglider mission and data processing can be found in *Webber et al.* [2014] and *Matthews et al.* [2014].

### 3. The DYNAMO Field Project: Case Study of Sequential CCKWs

During the DYNAMO field campaign [Yoneyama et al., 2013] three MJO events were intensively studied [DePasquale et al., 2014; Gottschalck et al., 2013; Johnson and Ciesielski, 2013; Kent et al., 2014]. The November 2011 MJO was associated with two sequential atmospheric Kelvin waves. Figures 1 and 2 present full and K14-filtered precipitation for this period, respectively. Prior to 21 November 2011 the central eastern Indian Ocean (80–95°E) is characterized by weak and scattered precipita-

tion. During late November 2011 an eastward propagating pattern of increased precipitation can be observed, associated with the November 2011 MJO. The November 2011 MJO event is marked by a red line in Figure 1. This corresponds to the  $0.9 \text{ mm d}^{-1}$  contour of MJO-filtered precipitation (eastward propagating zonal wave numbers 1–5, frequencies 1/96 to 1/30 cpd, following *Wheeler and Kiladis* [1999]). Precipitation within this MJO event intensifies in the form of two precipitation bands, which maintain higher phase speed than the MJO itself. Comparison between Figures 1 and 2 reveals that these two precipitation bands are, in fact, two sequential CCKWs associated with a strong signal (exceeding  $14 \text{ mm d}^{-1}$ ) in K14-filtered precipitation. Two CCKWs pass over 80°E, on 24 and 28 November 2011. Although the first of the CCKWs begins west of 40°E, the precipitation associated with it intensifies over the central Indian Ocean. The second CCKW rainfall event amplifies over the Indian Ocean around 55°E, and both CCKWs propagate in close proximity to each other over the central and eastern (55–100°E) Indian Ocean. It should be noted that some studies [Kerns and Chen, 2013] refer to only one CCKW and point to a meridional dynamical structure that temporarily suppressed convection at the equator. However, in our analysis we consistently rely on the CCKW trajectory database in which two sequential CCKW trajectories exist.

#### 3.1. Ocean Glider Observations of Two Sequential CCKWs at 80°E

The atmospheric and oceanic conditions during the second half of November 2011 at the Seaglider location at 80°E are now investigated (Figure 3). The Seaglider was located near the equator, between 3 and 4°S, enabling recognition and analysis of the equatorial CCKWs and the oceanic response to their forcing. Although this is outside the latitude band of 2.5°S to 2.5°N used in the CCKW analysis here, it is still well within the actual latitude band over which CCKWs are active [e.g., *Wheeler and Kiladis* 1999, Figure 7]. The latitude band of 2.5°S to 2.5°N was chosen to be consistent with the analysis of *Wheeler and Kiladis* [1999]. The whole time period presented in Figure 3 corresponds with the active phase of the MJO. However, two distinguishable anomalies manifested by wind bursts (TropFlux data; red line in Figure 3a) on 24 and 25 November and 29 November represent the two sequential CCKWs that were embedded in this MJO event.

Precipitation (TRMM 3B42 v7 data; blue line in Figure 3b) is also divided into two shorter periods, coincident with the passage of the two CCKWs. The first CCKW is manifested by increased precipitation on 24 November. The second CCKW can be associated with high precipitation rates on 28 November. Thus, periods 24 and 25 November and 28 and 29 November are consistent with the two sequential CCKWs at the Seaglider location.

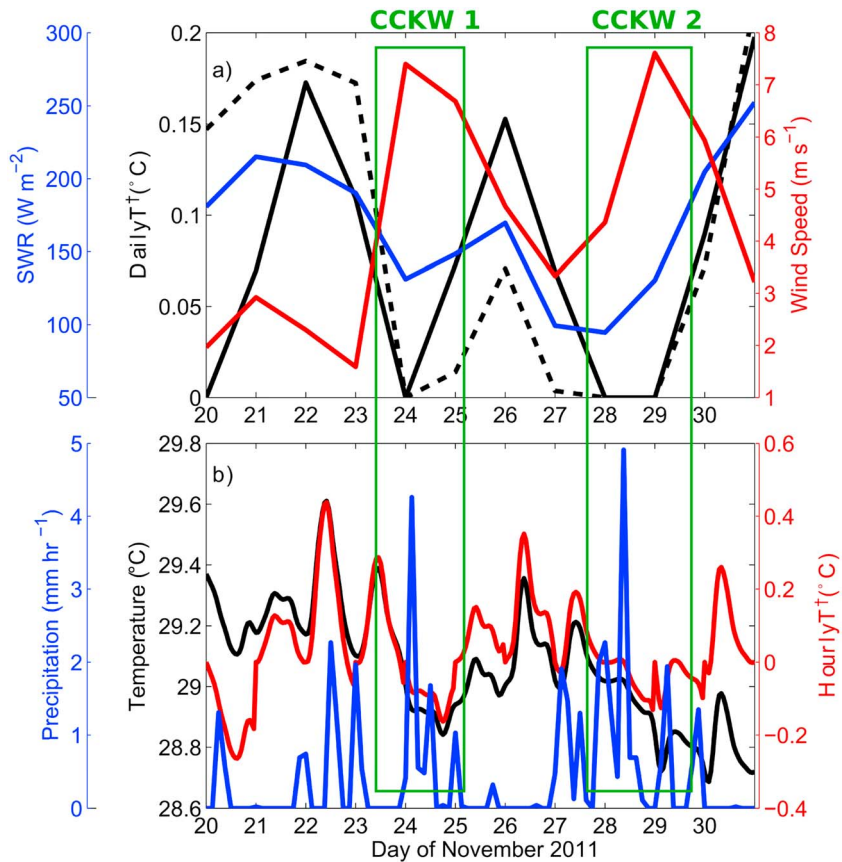


**Figure 3.** Time series at the Seaglider location for the period of 20 November to 1 December 2011. (a) Daily mean Seaglider  $T^+$  (black solid line), TropFlux derived  $T^+$  (black dashed line), TropFlux SWR (blue line), and TropFlux surface wind speed (red line). (b) Seaglider surface (0.5 m depth) temperature (black line) and  $T^+$  (red line), and TRMM precipitation (blue line). The green rectangles indicate the periods of the two sequential CCKWs.

These two periods also correlate with a systematic variation in the surface fluxes. During each of the CCKW convective periods decreased SWR (TropFlux data; blue line in Figure 3a), increased wind speed, and consequently increased latent heat flux (LHF) (TropFlux data; not shown) are observed. Between these convective periods, on 26 and 27 November decreasing wind speed and precipitation are apparent. On 26 November, solar radiation is increased as well.

The SST shows a general decrease of approximately  $0.5^{\circ}\text{C}$  in this 10 day period during the active phase of the MJO (black line in Figure 3b). At the same time some of the individual days exhibit a strong diurnal cycle, which has the same order of magnitude as the decreasing trend throughout that period.

On 24, 28, 29 November the diurnal cycle is suppressed. On these days both the daily maximum of  $T^+$  (red line in Figure 3b) and daily mean  $T^+$  (solid black line in Figure 3a) are close to  $0^{\circ}\text{C}$ . During the calm, nonconvective period (26 and 27 November) between sequential atmospheric CCKWs, the recovery of the strong diurnal signal in upper ocean temperature (red line in Figure 3b) is observed. High magnitudes of measured  $T^+$  are observed on 26 and 27 November, when the daily maximum exceeds  $0.35^{\circ}\text{C}$  and  $0.15^{\circ}\text{C}$ , respectively. The daily mean  $T^+$  for these two days exceeds  $0.05^{\circ}\text{C}$ . Hence, the diurnal cycle provides short-term daily pulses of increased SST, with magnitude comparable to the overall cooling trend.

Analysis of the Seaglider data from this case study suggests that CCKWs systematically interact with the upper ocean, but on shorter time scales than the MJO. The short-term impact on the SST is substantial and  $T^+$  is a useful metric of such short-term SST variability. Therefore, evaluation of  $T^+$  variability in other regions and for other periods, where direct upper ocean measurements are not available, should provide insight on air-sea interactions within equatorial convectively coupled waves. To this end, the black solid and dashed

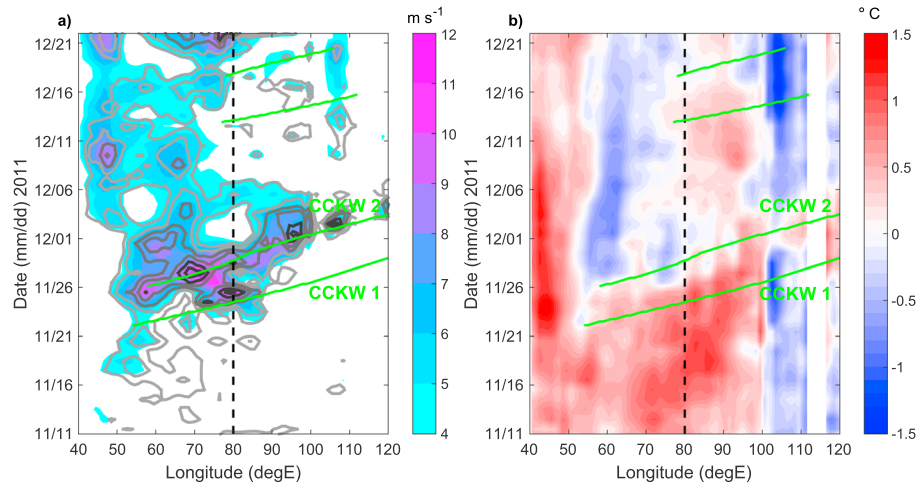


**Figure 4.** Hovmoller diagrams, averaged from 2.5°S to 2.5°N from 11 November to 21 December 2011, during the DYNAMO field experiment: (a) Daily mean wind speed (color shading, interval is  $1 \text{ m s}^{-1}$ , see legend; values below  $4 \text{ m s}^{-1}$  are masked out) and latent heat flux (line contour interval is  $20 \text{ W m}^{-2}$ ; black lines indicate values above  $180 \text{ W m}^{-2}$ , grey lines indicate values  $140$  and  $160 \text{ W m}^{-2}$ , light grey lines indicate values  $100$  and  $120 \text{ W m}^{-2}$ ; contours representing values below  $100 \text{ W m}^{-2}$  are omitted), (b) daily mean SST anomaly (color shading, interval is  $0.1^\circ\text{C}$ , see legend). Green lines show CCKW trajectories; black dashed lines indicate location of the Seaglider.

lines in Figure 3a show the daily averaged  $T^{\dagger}$  measured in situ by the Seaglider and the derived  $T^{\dagger}$  index described in section 2.4. It can be seen that the derived index captures the variability in the observed index associated with the sequential CCKW passage. It should be noted that although some discrepancies between observations and calculated index are visible (i.e., on 20 and 21 November) the overall dependence on the atmospheric forcing is well reproduced. Furthermore, the correlation coefficient calculated for the whole available record of Seaglider measurements and corresponding derived index has a value of 0.75. Thus, the derived  $T^{\dagger}$  provides a metric to study characteristics of upper ocean diurnal variability, in the absence of direct in situ measurements. In the following section we will use this metric, together with wind speed and LHF, to study air-sea interaction along the trajectories of the two sequential CCKWs in November 2011.

### 3.2. CCKW Impact on Surface Wind Speed, Latent Heat Flux, and SST

In this section the local analysis at the Seaglider location is extended across the Indian Ocean. We analyze the impact of the sequential CCKWs on the upper ocean for the entire wave trajectory and the impact of the associated CCKW convective activity on the surface wind speed, latent heat flux, and SST anomaly. We focus again on the two sequential CCKWs during November 2011. These CCKWs passed over  $80^\circ\text{E}$  (the Seaglider location) on 24 and 28 November 2011. Preceding the passage of these waves, during the suppressed phase of the MJO, wind speed and latent heat flux are small over the entire Indian Ocean basin, below  $4 \text{ m s}^{-1}$  and  $80 \text{ W m}^{-2}$ , respectively (Figure 4a).

The passage of the two CCKWs embedded in the active MJO between 21 November and 1 December is characterized by eastward propagation of an area of increased wind speed (above  $7 \text{ m s}^{-1}$ ) and increased LHF (above  $140 \text{ W m}^{-2}$ ; Figure 4a). During the transition period between the two sequential Kelvin wave trajectories, areas of decreased wind speed and decreased latent heat flux are observed. Let us consider the longitude  $80^\circ\text{E}$ , for example. Prior to the approach of the first CCKW the wind speed is  $3\text{--}4 \text{ m s}^{-1}$  and LHF is  $60\text{--}80 \text{ W m}^{-2}$ . During the first Kelvin wave passage wind speed increases above  $11 \text{ m s}^{-1}$  and LHF increases to  $120\text{--}140 \text{ W m}^{-2}$ . During the transition period wind speed decreases to  $6\text{--}7 \text{ m s}^{-1}$  and LHF decreases to  $40\text{--}60 \text{ W m}^{-2}$ . During the second Kelvin wave passage wind speed increases to  $10\text{--}11 \text{ m s}^{-1}$  and LHF increases to  $110\text{--}120 \text{ W m}^{-2}$ .

The SST decreases during the period when the two sequential CCKWs propagate through the central eastern Indian Ocean (Figure 4b). Prior to the first of the sequential CCKWs the SST exhibits a positive anomaly of the order of  $1^\circ\text{C}$ . After the passage of the second of the sequential CCKWs the SST anomaly is approximately  $0^\circ\text{C}$  over the eastern Indian Ocean. Negative SST anomalies after the second CCKW event are observed around

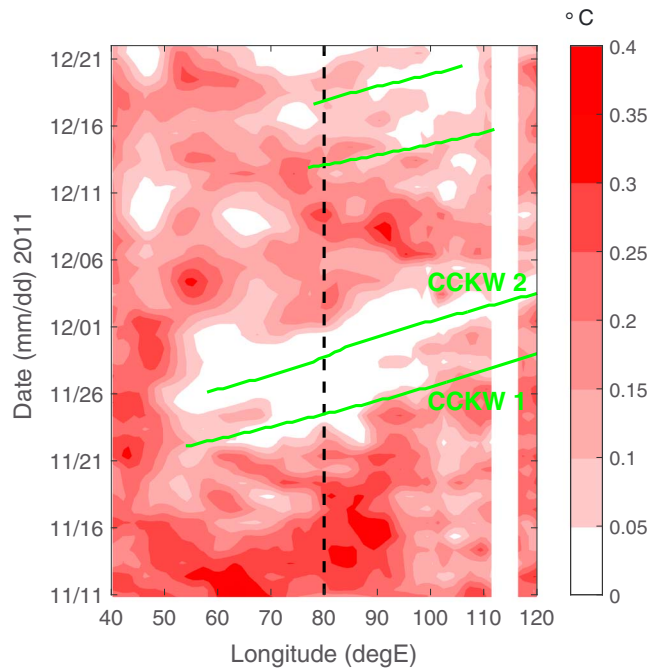


**Figure 5.** Hovmoller diagram of derived diurnal cycle of SST (daily mean  $T^{\dagger}$ , color shading interval is  $0.05^{\circ}\text{C}$ , see legend), averaged from  $2.5^{\circ}\text{S}$  to  $2.5^{\circ}\text{N}$  from 11 November to 21 December 2011, during the DYNAMO field experiment. Blue lines show CCKW trajectories; black dashed line indicates location of the Seaglider.

$60^{\circ}\text{E}$ , where increased values of surface wind speed persist after the convective wave passage, and around  $75^{\circ}\text{E}$ , where the ocean has been exposed to the strongest wind burst along the second CCKW trajectory. At  $80^{\circ}\text{E}$  this change in the SST anomaly occurs between 24 and 30 November. Although the rapid decrease in SST is associated with the CCKW activity, there is no characteristic short-term variability associated with each wave individually, as was observed for wind speed and LHF. That is likely because of the relatively short time scale of the atmospheric forcing variability associated with a CCKW passage and the large heat capacity of the oceanic mixed layer. Similarly, an asymmetric SST response, with much larger amplitude, is often observed during the passage of a tropical cyclone; wind-induced entrainment causes a decrease of the SST within a day or two [Price *et al.*, 1986], but recovery to the prestorm conditions may take up to several weeks [Mrvaljevic *et al.*, 2013].

### 3.3. CCKW Impact on Diurnal Cycle of SST

The Seaglider observations showed that SST decreased by approximately  $0.3^{\circ}\text{C}$  in 10 days during the passage of the two sequential CCKWs (black line in Figure 3b). However, some individual days exhibited a strong diurnal cycle, causing a short-term SST increase of the same magnitude. Here we use derived daily mean  $T^{\dagger}$  to investigate the relationship between the diurnal cycle of SST and CCKW activity over the Indian Ocean (Figure 5). The derived daily mean  $T^{\dagger}$  is high ( $0.25\text{--}0.30^{\circ}\text{C}$ ) over the entire Indian Ocean basin during the 11–21 November time period. This is the period of heat gain by the ocean and MJO suppressed phase.

The period between 21 November and 1 December is characterized by decreased upper ocean diurnal variability as measured by the derived  $T^{\dagger}$  (less than  $0.05^{\circ}\text{C}$ ). Eastward propagation of that signal is also visible. This period is dominated by the November MJO event.  $T^{\dagger}$  is suppressed to near zero during the passage of each of the two sequential CCKWs. However, areas of increased  $T^{\dagger}$  (to  $0.10^{\circ}\text{C}$ ) coincide with the transition period between the two sequential Kelvin waves, so the recovery of the diurnal variability is apparent shortly after wave passage. In comparison with the daily mean SST anomaly, analyzed in Figure 4b, the magnitude of the upper ocean temperature diurnal cycle increases much faster after the second of the sequential CCKW; only two days after passage of the second CCKW,  $T^{\dagger}$  is back to high values of  $0.20\text{--}0.25^{\circ}\text{C}$ .

Analysis of derived  $T^{\dagger}$  is consistent with the conclusion from Matthews *et al.* [2014] that within the active MJO phase the upper ocean diurnal cycle is not entirely obliterated by convective activity but can develop on certain days in certain areas. The variability of the diurnal cycle within the active phase of the November MJO event is correlated with the two sequential CCKWs associated with this MJO. Hence, the diurnal cycle can be suppressed quickly but also recovers quickly. At the same time, SST undergoes a more persistent decrease. This can be interpreted as a slower, intraseasonal change due to the active MJO envelope. However, in the multiscale framework being used here, the cumulative effect of the sequential CCKW events embedded within the MJO envelope is a substantial part of the intraseasonal change in SST. Hence, the short time scale effect of the CCKWs rectifies to produce a longer time scale (intraseasonal) SST change.

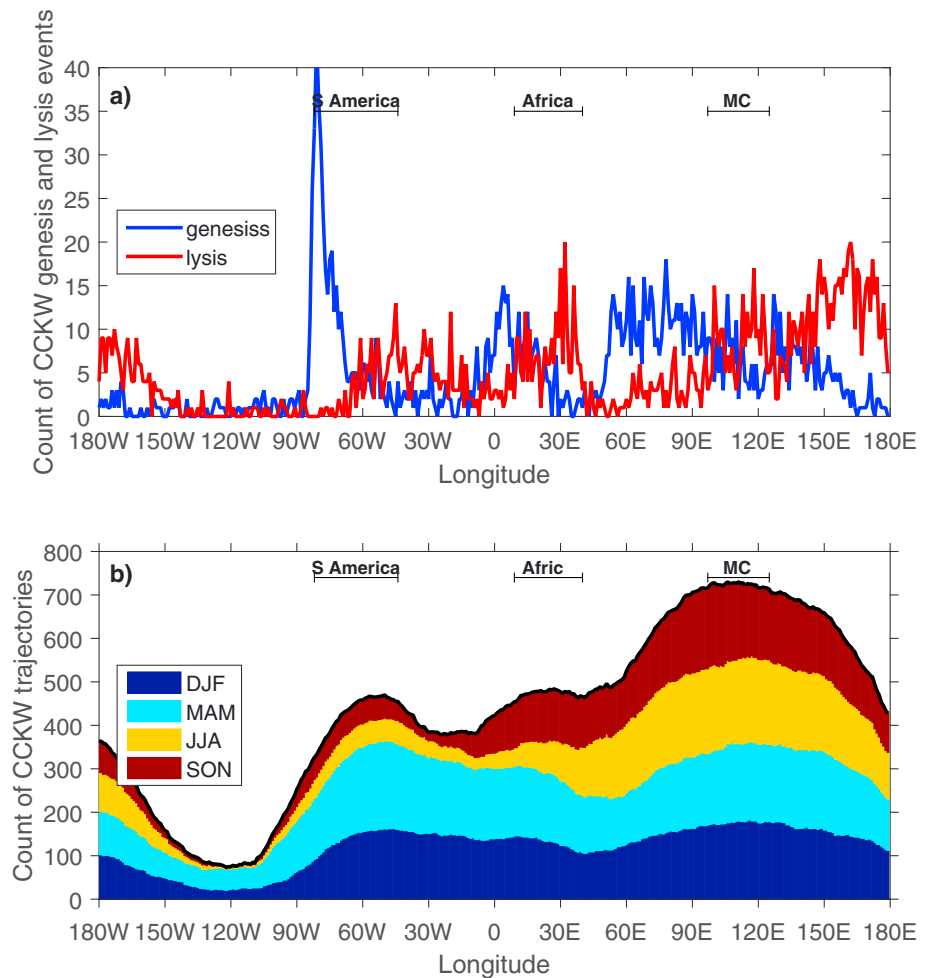


**Figure 6.** (a) Zonal distribution of trajectory’s beginning (genesis; blue line) and end (lysis; red line). (b) Number of active Kelvin wave trajectories passing through each longitude, stratified by season. Horizontal lines indicate locations of the South America, Africa, and Maritime Continent.

#### 4. Composite Analysis of Air-Sea Interactions in CCKWs

##### 4.1. CCKW Statistics

Following the case study of the CCKWs in the Indian Ocean in November 2011 during DYNAMO, we now carry out a climatological assessment of CCKWs and their air-sea interactions across the entire Tropics, using the CCKW Eulerian and Lagrangian databases. Statistics include areas of initiation and termination, frequency of occurrence, and dependence of occurrence on seasonal and intraseasonal variability of rain events associated with CCKWs.

The two databases contain 1840 CCKW trajectories that occurred between January 1998 and December 2012. There are large zonal asymmetries in the distribution of the beginning (genesis) and end (lysis) longitudes of rain events associated with individual CCKW trajectories (Figure 6a). In the central and eastern Indian Ocean (50–100°E), CCKW genesis is high ( $11 \pm 3$  initiations in each 1° longitude bin), and lysis is low ( $3 \pm 2$  terminations). Moving eastward over the Maritime Continent and into the western Pacific, CCKW genesis decreases to near zero at the dateline and lysis increases to a maximum at 160°E. Across the central and eastern Pacific (150–90°W), both genesis and lysis are very low. However, over the western seaboard of South America, genesis increases rapidly to the highest values found in the Tropics (a maximum of 40 CCKW trajectories initiated at 83°W). The western Atlantic Ocean is generally a region of low CCKW genesis and medium lysis. Genesis increases in the eastern Atlantic at 0°E, and lysis then increases to the east over Africa.

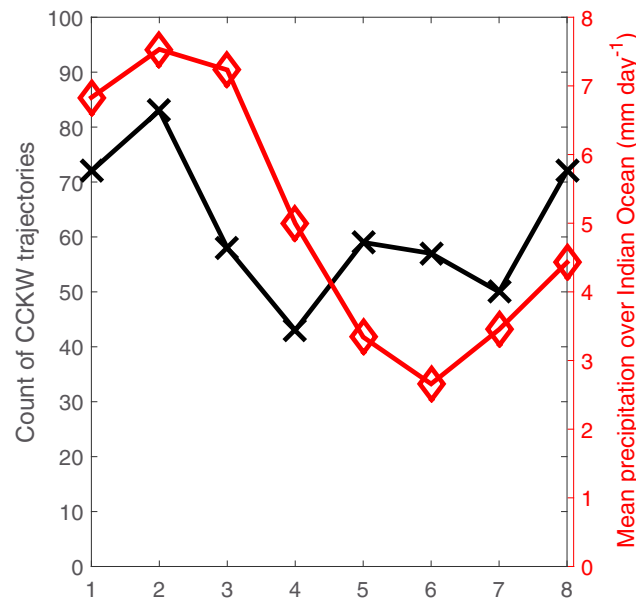


**Figure 7.** Number (sum) of active Kelvin wave trajectories in the Indian Ocean (40°E to 100°E) (black, crosses) and mean precipitation (red, diamonds) over Indian Ocean in each RMMI phase defined after *Wheeler and Hendon* [2004]. RMMI phases 2 and 3 mean MJO convection over the Indian Ocean. Calculations have been performed only for periods during which amplitude of the RMM index exceeds 1.

Out of the 1840 trajectories worldwide, 794 were active in the Indian Ocean basin defined as the area between 40°E and 100°E, making it the region of the highest CCKW activity observed in our data base. The total count of active CCKWs at each longitude (Figure 6b) shows three maxima of CCKW activity, corresponding to the three tropical continental regions: over South America at 55°W, Africa at 27°E, and the broad global maximum over the eastern Indian Ocean and the Maritime Continent between 97°E and 120°E where the total count of CCKWs exceeds 720. These zones of maximum CCKW activity are consistent with the genesis and lysis distributions discussed above, in that there is a genesis maximum to the west and a lysis maximum to the east of each zone, consistent with the eastward propagation of the CCKWs.

The data presented in Figure 6b are also stratified by season. It can be seen that in comparison with other

regions, the Indian Ocean basin and Maritime Continent have the largest number of summer (June–July–August, JJA) and autumn (September–November–October, SON) CCKWs. These two seasons account for more than 50% of all CCKW in that region. South America and Africa are dominated by winter (December–January–February, DJF) and spring (March–April–May, MAM) CCKWs. The number of CCKWs in DJF and MAM is relatively similar in the South America, Africa, Indian Ocean, and Maritime Continent regions. Hence, most of the regional differences in the number of CCKW are related to the JJA and SON seasons.

It should be noted that using our methodology, we consider a narrow equatorial band (2.5°S to 2.5°N) so we are excluding waves that propagate along the Intertropical Convergence Zone (ITCZ) that can be off the equator. In the Indian Ocean the CCKWs do tend to propagate along the equator but, for example, in the eastern Pacific the main “track” is slightly north [*Kiladis et al.*, 2009], especially during boreal summer [*Straub and Kiladis*, 2002]. Hence, part of the seasonal variability in this analysis may result from the seasonal migration of ITCZ. However, presented seasonal variability of CCKWs is consistent with *Roundy and Frank* [2004].

We have shown that the number of rainfall events associated with CCKW activity increases eastward through the Indian Ocean and achieves a global maximum over the Maritime Continent. We have also shown that the central and eastern Indian Ocean is a broad net source region of CCKWs associated with precipitation. Furthermore, the global maximum of intraseasonal convective variability is in the Indian Ocean [e.g., *Salby and Hendon* [1994]]. Therefore, it is natural to consider the effect of intraseasonal variability on the CCKW activity, as defined by our methodology.

The number of CCKW trajectories active in the Indian Ocean (black line in Figure 7) is highly correlated with the MJO cycle (red line in Figure 7). Mean precipitation rates over the Indian Ocean exceed 7 mm d<sup>-1</sup> during the convectively active Real-time Multivariate MJO index (RMMI) phases (1–3). Correspondingly, the peak CCKW activity is found in RMMI phase 2 (92 events). Conversely, RMMI phases 5–7 are the suppressed phases over the Indian Ocean, with mean precipitation less than 4 mm d<sup>-1</sup>; these phases only have approximately 50 recorded CCKW events. Cause and effect cannot be deduced from these data, but it is possible that the MJO active and suppressed phases provide environments that are conducive and unfavorable for CCKW activity, respectively. There may also be a role for CCKW activity to feed back onto the MJO, via modification of the atmosphere and ocean states.

#### 4.2. CCKW Surface Atmospheric Forcing

A lagged composite analysis of surface conditions was performed to assess the time-varying behavior of the CCKWs as they traverse the Indian Ocean (Figure 8). Five boxes were defined across the Indian Ocean, each of width 10° longitude (50–60°E; 60–70°E; 70–80°E; 80–90°E; 90–100°E). For each box, a composite was calculated from all the CCKW trajectories that were active across the whole box (to exclude trajectories that began or ended within the box). The day at which each trajectory was closest to the middle of the box was designated as day 0 for that trajectory in that box. An 11 day mean over each trajectory was calculated (from day –5 to day 5). This 11 day mean (which would include the climatological mean, seasonal cycle, and any interannual or intraseasonal variability) was subtracted from the data for each trajectory to leave the anomaly associated with that trajectory. Composites were then calculated from these anomalies.

Surface wind speed (Figure 8a) increases sharply during the passage of CCKWs in comparison with conditions 2 days before and after. There is marked zonal variability in this response. Although an increase in surface wind speed is evident at all longitudes between 50°E and 100°E, its magnitude is weakest over the western Indian Ocean and increases toward the east, to a maximum increase at 90–100°E of  $0.6 \text{ m s}^{-1}$  during the passage of CCKWs in comparison to conditions 2 days prior to its approach. After the CCKW passage, wind speed rapidly decreases to a minimum 2 days later. Hence, the passage of the CCKW lasts approximately 4 days. This sharp CCKW wind speed maximum is embedded in a more gradual longer-term increase in wind speed over the 11 day period shown in Figure 8a. This is likely because CCKW events preferentially occur in the convectively active phases of the MJO over the Indian Ocean, when the surface wind speed is generally increasing due to the spin up of surface westerly winds in the large-scale equatorial Rossby wave response to the MJO convection.

As latent heat flux anomalies are mainly due to changes in wind speed, the latent heat flux signal associated with the CCKWs (Figure 8b) also shows a strong peak on day 0, with rapid decay in the 2 days before and after the CCKW passage. Peak latent heat flux anomalies are again over the eastern Indian Ocean, at  $13 \text{ W m}^{-2}$ . The latent heat flux also shows a general slow increase over the 11 day period centered on the CCKW passage, likely related to the MJO changes in wind speed discussed above.

#### 4.3. CCKW Surface Ocean Response

The increase in wind speed and latent heat flux due to the passage of the CCKWs are likely to lead to a decrease in sea surface temperature, which may then feed back onto atmospheric convection. To that end we analyze the TropFlux SST data for which the seasonal cycle has been removed. The composite mean SST anomaly does show a very clear decrease of up to  $0.08^\circ\text{C}$  between days –1 and 1 (Figure 8c) as the CCKW passes through. Before day –1 and after day 1 the SST exhibits only minor variability. The SST response is stronger in the central and eastern Indian Ocean than in the western Indian Ocean. The SST does not recover after the passage of the CCKW. Hence, it appears that the CCKW has a long-lasting influence on the underlying ocean that will rectify onto longer time scales such as the MJO.

The passage of the CCKWs also has a large and coherent impact on the amplitude of the diurnal cycle of SST (Figure 8d). This reduction in surface diurnal warm layer development is also strongest in the eastern Indian Ocean, where the SST diurnal cycle amplitude is reduced by nearly  $0.08^\circ\text{C}$  at the peak of the CCKW passage (day 0 in Figure 8d), compared to 2 days before. As with SST before day –2 and after day 2, only minor and incoherent variability in the diurnal cycle of SST is observed. The composite amplitude change in the diurnal cycle of temperature during the CCKW passage is comparable the overall change in SST due to the CCKW passage as previously presented in the DYNAMO case study ( $0.12^\circ\text{C}$  for CCKW2 in Figure 3). Hence, it appears likely that there will be significant scale interactions between the diurnal cycle and the longer-term SST changes. The diurnal cycle of SST recovers quickly after the passage of the CCKW (the amplitude at day 2 is very similar to the amplitude at day –2).

#### 4.4. CCKW Atmospheric Boundary Layer Response

The variability of the ocean surface, forced by CCKWs, will feed back onto the atmospheric boundary layer. The CCKW composite 2 m air temperature anomaly (Figure 8e) has a temporal structure similar to that observed for the diurnal cycle of SST (Figure 8d). It drops by about  $0.5^\circ\text{C}$  during the CCKW passage and recovers within 2 days to pre-CCKW levels. It maintains nearly constant levels prior to day –2 and after day 2. It is interesting that the air temperature and diurnal cycle of the SST behave so similarly. Our calculation

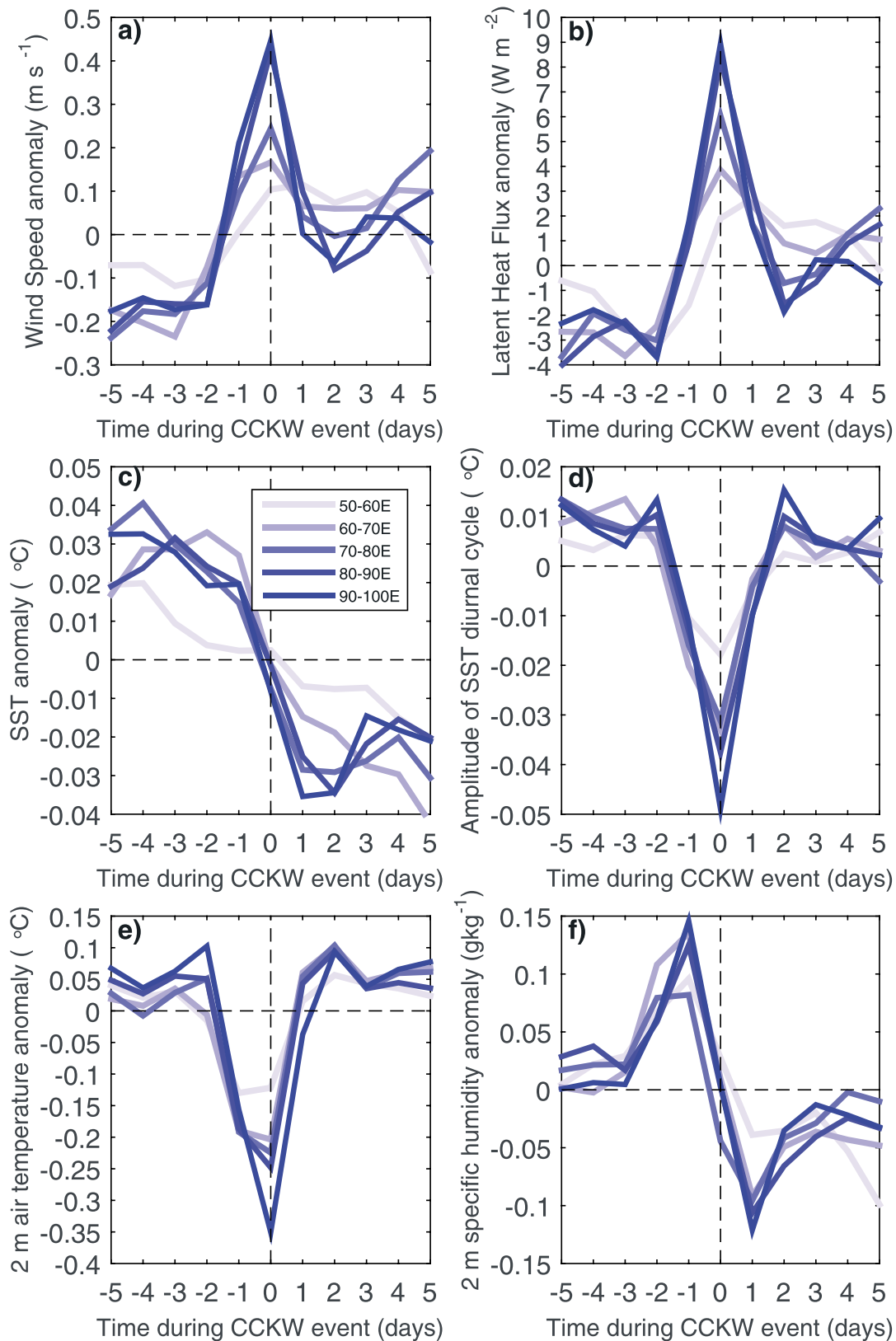


**Figure 8.** Composite lagged anomalies of (a) wind speed ( $m s^{-1}$ ), (b) latent heat flux ( $W m^{-2}$ ), (c) SST ( $^{\circ}C$ ), (d) diurnal cycle of SST (daily mean  $T^{\dagger}$ ) ( $^{\circ}C$ ), (e) air temperature at 2 m height ( $^{\circ}C$ ), and (f) specific humidity at 2 m height ( $g kg^{-1}$ ) for CCKWs active in the Indian Ocean at different longitude sectors (see key on Figure 8c). Time lag (horizontal axis) is relative to the passage of the Kelvin wave through that longitude sector.

of the diurnal cycle of SST is largely independent of the TropFlux SST data. Hence, the similarity between the two suggests that the diurnal cycle at the ocean surface is an important factor for driving the near-surface air temperature variability.

The variability of specific humidity at 2 m height (Figure 8f) during the CCKW passage has a different structure. Prior to the CCKW approach, it rapidly increases and reaches a maximum of  $0.15 \text{ g kg}^{-1}$  above the constant pre-CCKW level at 1 day before the CCKW passage. During the CCKW passage, it decreases by nearly  $0.3 \text{ g kg}^{-1}$ . The minimum specific humidity is observed 1 day after the CCKW passage, after which it increases and stabilizes at a level slightly ( $\sim 0.05 \text{ g kg}^{-1}$ ) below its pre-CCKW value. This variability is zonally coherent. The composite variability of the specific humidity presented here is consistent with previous studies reporting rapid moistening prior to the CCKW approach and a post CCKW drying in the lower troposphere [Kiladis *et al.*, 2009]. Hence, although the post-CCKW air temperature quickly returns to its pre-CCKW level, the specific humidity stabilizes below its pre-CCKW level. This can be linked to the longer-lasting SST decrease. This post-CCKW dryness may then also contribute to the increased post-CCKW latent heat flux (Figure 8b).

## 5. Summary and Discussion

The atmosphere-ocean interactions during the propagation of CCKWs were investigated using in situ measurements from the DYNAMO field project and CCKW trajectories contained in the database developed for this project. The direct impact of the Kelvin wave activity on the ocean surface fluxes and subsurface temperature variability were evaluated.

Over 1800 CCKWs were identified globally based on TRMM data for the 15 year period between 1998 and 2012. Over 40% of CCKW trajectories were active over the Indian Ocean basin. CCKW activity in that region is highly affected by intraseasonal variability associated with the MJO. The number of CCKWs in the Indian Ocean is largest during periods of active MJO convection and decreases by nearly 50% when MJO convection is suppressed.

Atmosphere-ocean interactions during CCKW events are characterized by variability in the air-sea fluxes, forced mainly by changes in wind speed and cloudiness associated with the convective envelope of the Kelvin wave. Increased surface wind speed and reduced solar insolation, due to increased convective activity, force significant changes in latent heat flux, lower atmospheric boundary layer humidity and temperature, SST, and the upper ocean diurnal cycle. Typical variability associated with a CCKW passage lasts approximately 4 days. During this period, wind speed increases by approximately  $0.6 \text{ m s}^{-1}$  and latent heat flux increases by  $13 \text{ W m}^{-2}$ . Both wind speed and latent heat flux decrease after the wave passage, but to a level that exceeds that observed before the CCKW.

The upper ocean response to the atmospheric forcing, composed of the combined effect of increased wind speed and cloudiness, is such that the magnitude of the upper ocean temperature diurnal cycle decreases by  $0.07^\circ\text{C}$  in comparison to pre-CCKW conditions, and daily SST decreases by  $0.1^\circ\text{C}$ . The magnitude of the diurnal cycle returns to the pre-CCKW level within 2 days after an event, whereas the bulk SST negative anomaly persists longer. It should be noted that our DYNAMO case study shows SST decrease of about  $0.3^\circ\text{C}$  for each of the sequential CCKWs. The difference between composite and case study SST variability can be attributed to the case dependency similar to the observed for the MJO during DYNAMO [Fu *et al.*, 2014].

Variability in the air-sea fluxes and upper ocean temperature structure can be linked to variability in the atmospheric boundary layer temperature and humidity. The atmospheric boundary layer temperature decreases by  $0.4^\circ\text{C}$  during a CCKW passage, with a subsequent return to the pre-CCKW level. This variability is similar to the observed behavior of the upper ocean temperature diurnal cycle, which may indicate the influence of the upper ocean short-term variability on the lower troposphere temperature changes. The specific humidity variability is more complicated. However, our observations agree with previous studies [Kiladis *et al.*, 2009; Straub and Kiladis, 2003], which reported an increase in specific humidity with maximum values achieved 1 day before the peak of convection, followed by a rapid decrease and minimum value observed 1 day after the CCKW passage. In the following days, the specific humidity slightly increases but remains below pre-CCKW values.

The observed CCKW variability exhibits a strong zonal modulation. The magnitude and coherence of the ocean flux response to the CCKW passage is weakest over the western Indian Ocean, and increases eastward.

This can be linked to the structure and coherence of the organized convective envelopes across the Indian Ocean. Roundy [2008] showed that the circulation that links low level westerly anomalies and the latent heat release in deep moist convection in CCKWs amplifies as the wave crosses the Indian Ocean.

Although the strongest and most coherent response to the passage of a CCKW occurs over a relatively short 5 day period, there are also residual changes in the levels of SST, latent heat flux, and specific humidity at 2 m that persist for longer period. Therefore, air-sea flux variability associated with CCKWs over the Indian Ocean can rectify onto longer, interseasonal time scales by explaining part of the observed air-sea interactions and low-level tropospheric temperature and humidity associated with MJO envelope. Given that there is high CCKW activity during the active phase of the MJO, this implies that a substantial component of the intraseasonal variability is due to the individual Kelvin waves. For example, our analysis of the Seaglider measurements during the DYNAMO field campaign (Figure 3) show an SST decrease of approximately 0.5°C over 10 days during the onset of an active MJO. This SST decrease was mainly due to the effect of two sequential CCKWs associated with this MJO event. We would argue that this is not an outlier, but is rather a typical example of short-term variability associated with CCKWs rectifying onto the intraseasonal time scale. The typical SST decrease associated with the MJO over the central eastern Indian Ocean is of the order of 0.3°C [Matthews *et al.*, 2010; Shinoda *et al.*, 1998]. The SST decrease associated with a single CCKW is of the order of 0.1°C (Figure 8), and more than one CCKW is often embedded in a single MJO event (Figure 1). Thus, interactions between CCKWs and air-sea fluxes can contribute 50% or more to the SST variability associated with an MJO.

Finally, our results suggest that CCKWs can contribute to a gradual increase of atmospheric moisture. Although specific humidity decreases after a CCKW passage and SST is lower than before an event, an increased wind speed combined with high diurnal cycle of SST can contribute to gradual rebuilding of atmospheric boundary layer moisture (Figure 8b). Similar low-level moisture buildup has been shown, for example, in Figure 8 of Kiladis *et al.* [2009] for CCKWs over the central Pacific.

Observed scale interactions between CCKWs and lower frequency MJO events have been shown here to be an important component of the tropical ocean-atmosphere system. It is an open question as to how well these processes are simulated in models, and whether a poor or absent representation of these processes in a simulation degrades a model forecast or climate projection.

#### Acknowledgments

D.B.B. has been supported by Poland's National Science Centre (Narodowe Centrum Nauki) (decision 2012/07/N/ST10/03303). M.K.F. and P.J.F. have been supported by ONR DRI (Unified Physical Parameterization for Extended-Range Prediction); Analysis of the DYNAMO field campaign data has been supported by the Office of Naval Research under program element 601153N.

#### References

- Bernie, D. J., E. Guilyardi, G. Madec, J. M. Slingo, S. J. Woolnough, and J. Cole (2008), Impact of resolving the diurnal cycle in an ocean-atmosphere GCM. Part 2: A diurnally coupled CGCM, *Clim. Dyn.*, 31(7–8), 909–925.
- DePasquale, A., C. Schumacher, and A. Rapp (2014), Radar observations of MJO and Kelvin wave interactions during DYNAMO/CINDY2011/AMIE, *J. Geophys. Res. Atmos.*, 119, 6347–6367, doi:10.1002/2013JD021031.
- Flatau, M. K., P. J. Flatau, J. Schmidt, and G. N. Kiladis (2003), Delayed onset of the 2002 Indian monsoon, *Geophys. Res. Lett.*, 30(14), 1768, doi:10.1029/2003GL017434.
- Flatau, M., P. J. Flatau, P. Phoebus, and P. P. Niller (1997), The feedback between equatorial convection and local radiative and evaporative processes: The implications for intraseasonal oscillations, *J. Atmos. Sci.*, 54(19), 2373–2386.
- Fu, X. H., and B. Wang (2004), Differences of boreal summer intraseasonal oscillations simulated in an atmosphere-ocean coupled model and an atmosphere-only model, *J. Clim.*, 17(6), 1263–1271.
- Fu, X., W. Wang, J.-Y. Lee, B. Wang, K. Kikuchi, J. Xu, J. Li, and S. Weaver (2014), Distinctive roles of air-sea coupling on different MJO events: A new perspective revealed from the DYNAMO/CINDY field campaign, *Mon. Weather Rev.*, 143(3), 794–812.
- Gottschalck, J., P. E. Roundy, C. J. Schreck III, A. Vintzileos, and C. Zhang (2013), Large-scale atmospheric and oceanic conditions during the 2011–12 DYNAMO field campaign, *Mon. Weather Rev.*, 141(12), 4173–4196.
- Huffman, G. J., R. F. Adler, D. T. Bolvin, G. Gu, E. J. Nelkin, K. P. Bowman, Y. Hong, E. F. Stocker, and D. B. Wolff (2007), The TRMM multisatellite precipitation analysis (TMPA): Quasi-global, multiyear, combined-sensor precipitation estimates at fine scales, *J. Hydrometeorol.*, 8(1), 38–55.
- Johnson, R. H., and P. E. Ciesielski (2013), Structure and properties of Madden-Julian oscillations deduced from DYNAMO sounding arrays, *J. Atmos. Sci.*, 70(10), 3157–3179.
- Kent, E. C., D. I. Berry, J. Prytherch, and J. B. Roberts (2014), A comparison of global marine surface-specific humidity datasets from in situ observations and atmospheric reanalysis, *Int. J. Climatol.*, 34(2), 355–376.
- Kerns, B. W., and S. S. Chen (2013), Equatorial dry air intrusion and related synoptic variability in MJO initiation during DYNAMO, *Mon. Weather Rev.*, 142(3), 1326–1343.
- Kiladis, G. N., M. C. Wheeler, P. T. Haertel, K. H. Straub, and P. E. Roundy (2009), Convectively coupled equatorial waves, *Rev. Geophys.*, 47, RG2003, doi:10.1029/2008RG000266.
- Klingaman, N. P., S. J. Woolnough, H. Weller, and J. M. Slingo (2011), The impact of finer-resolution air-sea coupling on the intraseasonal oscillation of the Indian monsoon, *J. Clim.*, 24(10), 2451–2468.
- Majda, A. J., and B. Khouider (2004), A model for convectively coupled tropical waves: Nonlinearity, rotation, and comparison with observations, *J. Atmos. Sci.*, 61(17), 2188–2205.

- Mapes, B., S. Tulich, J. Lin, and P. Zuidema (2006), The mesoscale convection life cycle: Building block or prototype for large-scale tropical waves?, *Dyn. Atmos. Oceans*, *42*(1–4), 3–29.
- Matthews, A. J., P. Singhruck, and K. J. Heywood (2010), Ocean temperature and salinity components of the Madden-Julian oscillation observed by Argo floats, *Clim. Dyn.*, *35*(7–8), 1149–1168.
- Matthews, A. J., D. B. Baranowski, K. J. Heywood, P. J. Flatau, and S. Sunke (2014), The surface diurnal warm layer in the Indian Ocean during CINDY/DYNAMO, *J. Clim.*, *27*(24), 9101–9122.
- McLay, J. G., M. K. Flatau, C. A. Reynolds, J. Cummings, T. Hogan, and P. J. Flatau (2012), Inclusion of sea-surface temperature variation in the U.S. Navy ensemble-transform global ensemble prediction system, *J. Geophys. Res.*, *117*, D19120, doi:10.1029/2011JD016937.
- Mrvaljevic, R. K., et al. (2013), Observations of the cold wake of Typhoon Fanapi (2010), *Geophys. Res. Lett.*, *40*, 316–321, doi:10.1029/2012GL054282.
- Nakazawa, T. (1988), Tropical super clusters within intraseasonal variations over the western Pacific, *J. Meteorol. Soc. Jpn.*, *66*(6), 823–839.
- Praveen Kumar, B., J. Vialard, M. Lengaigne, V. S. N. Murty, M. J. McPhaden, M. F. Cronin, F. Pinsard, and K. Gopala Reddy (2013), TropFlux wind stresses over the tropical oceans: Evaluation and comparison with other products, *Clim. Dyn.*, *40*(7–8), 2049–2071.
- Price, J. F., R. A. Weller, and R. Pinkel (1986), Diurnal cycling: Observations and models of the upper ocean response to diurnal heating, cooling, and wind mixing, *J. Geophys. Res.*, *91*(C7), 8411–8427, doi:10.1029/JC091iC07p08411.
- Roundy, P. E. (2008), Analysis of convectively coupled Kelvin waves in the Indian ocean MJO, *J. Atmos. Sci.*, *65*(4), 1342–1359.
- Roundy, P. E., and W. M. Frank (2004), A climatology of waves in the equatorial region, *J. Atmos. Sci.*, *61*(17), 2105–2132.
- Salby, M. L., and H. H. Hendon (1994), Intraseasonal behavior of clouds, temperature, and motion in the tropics, *J. Atmos. Sci.*, *51*(15), 2207–2224.
- Shinoda, T., H. H. Hendon, and J. Glick (1998), Intraseasonal variability of surface fluxes and sea surface temperature in the tropical western Pacific and Indian Oceans, *J. Clim.*, *11*(7), 1685–1702.
- Shinoda, T., T. G. Jensen, M. Flatau, and S. Chen (2013), Surface wind and upper-ocean variability associated with the Madden-Julian oscillation simulated by the Coupled Ocean–Atmosphere Mesoscale Prediction System (COAMPS), *Mon. Weather Rev.*, *141*(7), 2290–2307.
- Straub, K. H., and G. N. Kiladis (2002), Observations of a convectively coupled Kelvin wave in the eastern Pacific ITCZ, *J. Atmos. Sci.*, *59*(1), 30–53.
- Straub, K. H., and G. N. Kiladis (2003), The observed structure of convectively coupled Kelvin waves: Comparison with simple models of coupled wave instability, *J. Atmos. Sci.*, *60*(14), 1655–1668.
- Webber, B. G. M., A. J. Matthews, K. J. Heywood, J. Kaiser, and S. Schmidtke (2014), Seaglider observations of equatorial Indian Ocean Rossby waves associated with the Madden-Julian Oscillation, *J. Geophys. Res. Oceans*, *119*, 3714–3731, doi:10.1002/2013JC009657.
- Wheeler, M. C., and H. H. Hendon (2004), An all-season real-time multivariate MJO index: Development of an index for monitoring and prediction, *Mon. Weather Rev.*, *132*(8), 1917–1932.
- Wheeler, M., and G. N. Kiladis (1999), Convectively coupled equatorial waves: Analysis of clouds and temperature in the wavenumber-frequency domain, *J. Atmos. Sci.*, *56*(3), 374–399.
- Woolnough, S. J., F. Vitart, and M. A. Balmaseda (2007), The role of the ocean in the Madden–Julian Oscillation: Implications for MJO prediction, *Q. J. Roy. Meteorol. Soc.*, *133*(622), 117–128.
- Yoneyama, K., C. Zhang, and C. N. Long (2013), Tracking pulses of the Madden-Julian Oscillation, *Bull. Am. Meteorol. Soc.*, *94*(12), 1871–1891.
- Zeng, X., and A. Beljaars (2005), A prognostic scheme of sea surface skin temperature for modeling and data assimilation, *Geophys. Res. Lett.*, *32*, L14605, doi:10.1029/2005GL023030.